Bioactive Materials 16 (2022) 120–133

Contents lists available at ScienceDirect

Bioactive Materials

journal homepage: www.keaipublishing.com/en/journals/bioactive-materials

LIFU-responsive nanomedicine enables acoustic droplet vaporization-induced apoptosis of macrophages for stabilizing vulnerable atherosclerotic plaques

Jingxin Hou [a,1], Jun Zhou [a,1], Meiqi Chang [d], Guangcheng Bao [e], Jie Xu [a], Man Ye [a], Yixin Zhong [a], Shuling Liu [a], Junrui Wang [a], Wei Zhang [a], Haitao Ran [c], Zhigang Wang [c,**], Yu Chen [b,*], Dajing Guo [a,***]

[a] Department of Radiology, Second Affiliated Hospital of Chongqing Medical University, Chongqing, 400010, PR China
[b] Materdicine Lab, School of Life Sciences, Shanghai University, Shanghai, 200444, PR China
[c] Chongqing Key Laboratory of Ultrasound Molecular Imaging & Department of Ultrasound, Second Affiliated Hospital of Chongqing Medical University, Chongqing, 400010, PR China
[d] State Key Laboratory of High Performance Ceramics and Superfine Microstructure, Shanghai Institute of Ceramics, Chinese Academy of Sciences, Shanghai, 200050, PR China
[e] Department of Radiology, Children's Hospital of Chongqing Medical University, Chongqing, 400014, PR China

ARTICLE INFO

Keywords:
Vulnerable plaques
Acoustic droplet vaporization
Macrophages
Apoptosis
Nanomedicine

ABSTRACT

Due to the high risk of tearing and rupture, vulnerable atherosclerotic plaques would induce serious cardiovascular and cerebrovascular diseases. Despite the available clinical methods can evaluate the vulnerability of plaques and specifically treat vulnerable plaques before a cardiovascular event, but the efficiency is still low and undesirable. Herein, we rationally design and engineer the low-intensity focused ultrasound (LIFU)-responsive FPD@CD nanomedicine for the highly efficient treatment of vulnerable plaques by facilely loading phase transition agent perfluorohexane (PFH) into biocompatible PLGA-PEG-PLGA nanoparticles (PPP NPs) and then attaching dextran sulphate (DS) onto the surface of PPP NPs for targeting delivery. DS, as a typical macrophages-targeted molecule, can achieve the precise vaporization of NPs and subsequently controllable apoptosis of RAW 264.7 macrophages as induced by acoustic droplet vaporization (ADV) effect. In addition, the introduction of DiR and Fe_3O_4 endows nanomedicine with near-infrared fluorescence (NIRF) and magnetic resonance (MR) imaging capabilities. The engineered FPD@CD nanomedicine that uses macrophages as therapeutic targets achieve the conspicuous therapeutic effect of shrinking vulnerable plaques based on *in vivo* and *in vitro* evaluation outcomes. A reduction of 49.4% of vascular stenosis degree in gross pathology specimens were achieved throughout the treatment period. This specific, efficient and biosafe treatment modality potentiates the biomedical application in patients with cardiovascular and cerebrovascular diseases based on the relief of the plaque rupture concerns.

1. Introduction

Cardiovascular disease (CVD) is now one of the leading causes of death worldwide [1,2], and the majority of cardiovascular events, such as stroke and myocardial infarction, are caused by the rupture of vulnerable atherosclerotic plaques [3]. A large proportion of ruptured plaques exhibit less than 60% blood vessel stenosis, and an assessment of the risk of plaques based on the degree of blood vessel stenosis is still insufficient [4]. The current clinical treatments for atherosclerotic plaques mainly include lifestyle changes, cholesterol-lowering drugs, blood pressure surveillance, antithrombotic drugs, and surgical interventions [5–7]. Effective clinical methods and protocols have not been developed

Peer review under responsibility of KeAi Communications Co., Ltd.
* Corresponding author.
** Corresponding author.
*** Corresponding author.
E-mail addresses: wzg62942443@163.com (Z. Wang), chenyuedu@shu.edu.cn (Y. Chen), guodaj@163.com (D. Guo).
[1] These authors contributed equally to this work and should be considered co-first authors.

https://doi.org/10.1016/j.bioactmat.2022.02.022
Received 10 September 2021; Received in revised form 21 February 2022; Accepted 21 February 2022
Available online 3 March 2022

specifically for treating high-risk vulnerable plaques.

Macrophages have been selected as the therapeutic targets for atherosclerosis because they are closely related to plaque inflammation [8–10]. Compared with stable plaques, vulnerable plaques contain a significantly increased number of lipid-containing macrophages, which have been used as therapeutic targets to achieve the specific treatment of vulnerable plaques at risk of rupture [11–13]. Currently, most of the strategies used to induce apoptosis in macrophages are drug intervention. For example, statins [14] and methotrexate [15] have been loaded into nanoparticles (NPs) and delivered to plaque macrophages, but these drug-based methods exert relatively slow effects and poor controllability, which were mainly reflected in the lack of local specificity, the inability to achieve precise treatment and the possibility of systemic toxicity. Alternatively, Kalas W et al. used photosensitizers-loaded liposomes to achieve the photodepletion of macrophages [16], but the tissue-penetration capability of light waves was relatively low. Thus, the curative effect on deep tissue-seated lesions was limited. Moreover, the potential toxicity of photosensitizers hinders their further clinical translation [17,18]. It is highly necessary and urgent to develop alternative and efficient protocols with easy-performing, accurate, biosafe, and effective features.

On this ground, we herein propose a new treatment strategy for vulnerable plaques by employing acoustic droplet vaporization (ADV) caused by low-intensity focused ultrasound (LIFU) irradiation [19–21]. The concept of ADV was proposed by Kripfgans et al. [22] in 2000. It refers to the liquid fluorocarbon NPs in the acoustic field, which undergo regular compression and expansion under the action of ultrasonic waves. The internal pressure changes cyclically with the variation of external sound pressure. When the internal pressure drops below the external pressure (the vapor pressure of water), the liquid-gas phase transformation of liquid fluorocarbon emerged. ADV is implemented mainly by liquid fluorocarbons, such as perfluorhexane (PFH), perfluoropentane (PFP), *etc.*, which are wrapped in various materials and transformed into gaseous phase after ultrasonic activation, thus providing a long cycle and triggering contrast agent. The liquid core underwent a phase change to gas during the ultrasound (US) activation, which features stronger tissue penetration than conventional light [23], aiming to induce the apoptosis of macrophages in vulnerable plaques to achieve the specific and efficient treatment of these plaques. Previously, our research group discussed the mechanism and efficacy of ADV caused by LIFU irradiation for the treatment of another vascular disease, thrombosis [24,25]. During ADV, a series of active dynamic processes, such as oscillation, expansion, contraction, and even the collapse of tiny bubbles in the liquid, are generated by the action of sound waves, thereby inducing some specific phenomena such as chemical reactions, luminescence, and subharmonics [26,27], which potentially result in damage inside the thrombus, leading to the thrombus loosening and improving the efficacy of subsequently administered thrombolytic drugs. In theory, ADV is potentially useful for treating vulnerable plaques by damaging the ultrastructure of macrophages, however, tears inside the plaque and the loose plaque structure induced by ADV without appropriate adjustments would elevate the risk of plaque rupture and thromboembolism and aggravate the progression of the disease [28,29]. As noted above, ADV is a double-edged sword for vulnerable plaques, therefore the determination of the appropriate treatment conditions is highly critical.

Perfluorocarbon (PFC) phase-transition emulsion droplets are promising materials in the field of biomedicine due to the easily controllable transformation of these liquid droplets into microbubbles using localised heat or via acoustic droplet vaporization [27], and the accompanying ADV effects have also been broadly used in the treatment of various diseases, such as tumors and thrombus [24,30]. Among PFCs, perfluorohexane (PFH, bp ~ 56 °C) features higher stability *in vivo* than perfluoropentane (PFP, bp ~ 29 °C) due to the higher boiling point [31]. In addition, various molecular bioimaging technologies play an increasingly prominent role in the diagnosis of cardiovascular diseases [32–34]. Among them, near-infrared fluorescence (NIRF) possesses high sensitivity but insufficient spatial resolution features. On the contrary, magnetic resonance (MR) is a non-invasive technique with superior tissue penetration depth and detailed soft tissue contour capability, but its sensitivity needs to be improved. Therefore, multimodal molecular imaging combined with NIRF imaging and MR imaging is expected to complement each other and realize early and accurate diagnosis of atherosclerotic plaques, which benefits the acquiring of more detailed information for clinical intervention. Furthermore, dextran sulphate (DS) can recognize and bind to type A scavenger receptor (SR-A), which is only expressed on activated macrophages [35], therefore DS can assist NPs to target macrophages in vulnerable plaques.

Herein, PLGA-PEG-PLGA was selected as the carrier of the composite nanosystem. MR contrast agent Fe_3O_4 (F), the phase transition material PFH (P), and the NIRF contrast agent 1,1′-dioctadecyl-3,3,3′,3′-tetramethylindotricarbocyanine iodide (DiR) (D) were co-loaded into the nanosystem. DS, which specifically targets SR-A expressed on the surface of macrophages, was attached onto the surface of the PPP NPs via electrostatic absorption with the assistance of chitosan (CS) (C), achieving the precise construction of LIFU-responsive and theranostic nanomedicine FPD@CD NPs for vulnerable plaques. We conducted a detailed study to explore the optimal treatment conditions for ADV including LIFU irradiation intensity and plaque stability. The mechanism of ADV in the treatment of vulnerable plaques, the treatment condition-induced effects, the specific changes in plaque, the distribution, and *in vivo* biological safety were explored systematically. The preparation process of the final FPD@CD nanomedicines and the effect of ADV on RAW 264.7 cells and vulnerable atherosclerotic plaques were illustrated in Scheme 1. The successful implementation of this research provides a new, non-invasive, time-space controllable treatment paradigm for vulnerable plaque under the monitoring of NIRF and MR, which features high clinical translation potential for the treatment of patients with cardiovascular and cerebrovascular diseases.

2. Materials and methods

2.1. Materials

PLGA-PEG-PLGA (lactide:glycolide = 75:25, with a molecular weight of 16,000 Da for PLGA and 2000 Da for PEG) was purchased from Daigang Bio Engineer Co., Ltd. (Shandong, China). Iron oxide NPs (Fe_3O_4, 10 nm) modified with oleic acid were obtained from Ocean Nano Technology Co., Ltd. (Springdale, AR, USA). PFH was obtained from J&K Scientific Co., Ltd. (Beijing, China). CS with a molecular weight of 50,000 Da was received from Macklin Biochemical Co., Ltd. (Shanghai, China). DS with a molecular weight of 5000 Da was provided by Aladdin Reagent Co., Ltd. (Shanghai, China). 4′,6-diamidino-2-phenylindole (DAPI), 1,1′ -dioctadecyl-3,3,3′,3′ -tetramethylindocarbocyanine perchlorate (DiI), DiR, calcein-AM and propidium iodide (PI) were obtained from Sigma-Aldrich Chemical Co., Ltd. (St. Louis, MO, USA). The Cell Counting Kit-8 (CCK-8) assay kit was purchased from Dojindo Laboratories (Kumamoto, Japan). The F4/80 antibody was purchased from Bioss Biotechnology Co., Ltd. (Beijing, China). Enzyme-linked immunosorbent assay (ELISA) kits, TdT-mediated dUTP nick-end labeling (TUNEL) apoptosis assay kits were purchased from Boster Biological Technology Co., Ltd. (Wuhan, China).

2.2. Preparation of Fe_3O_4-PFH-DiR@CS-DS NPs

The preparation method of FPD@CD NPs is similar to that in our previous article [21]. A solvent evaporation method was used to prepare the FPD NPs first. After CH_2Cl_2 (2 mL) was added to dissolve PLGA-PEG-PLGA (50 mg), the Fe_3O_4 NPs (200 μL, 25 mg mL^{-1}) and DIR (0.1 mg) were added. DS was attached to the surface of the FPD NPs via electrostatic absorption with the assistance of CS. Specifically, we first prepared FPD@C NPs. DS (10 mg) was added to the FPD@C dispersion

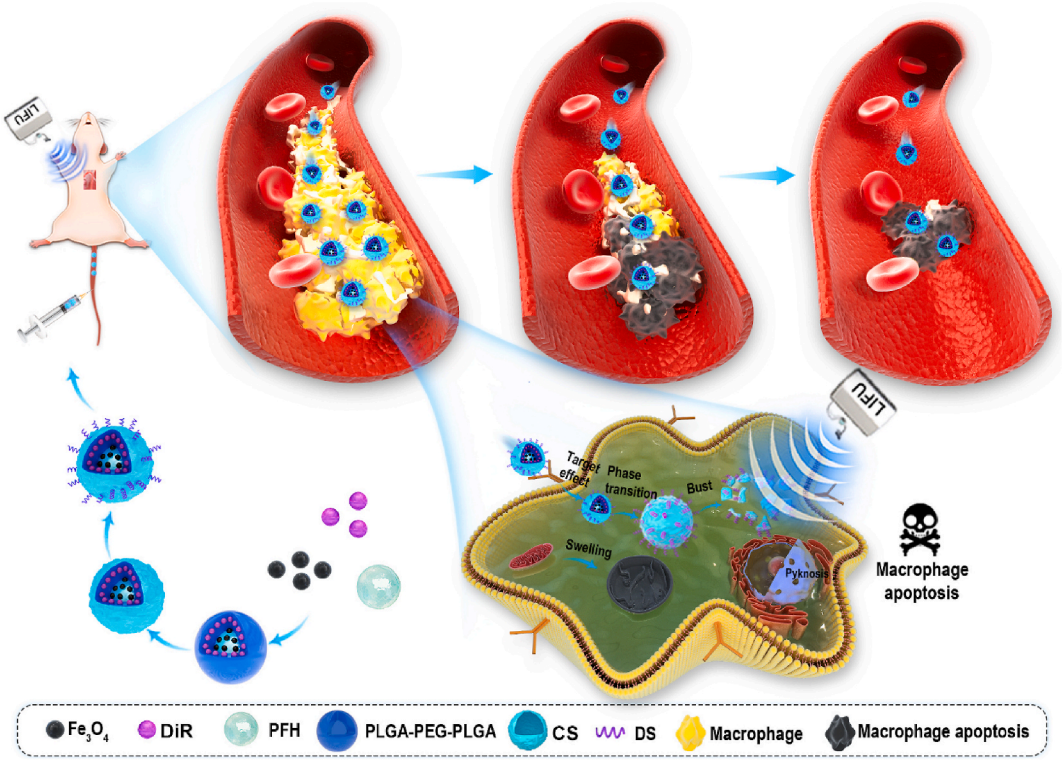

Scheme 1. Schematic illustration of the preparation of the FPD@CD NPs and the effect of ADV on RAW 264.7 cells and vulnerable atherosclerotic plaques.

under an ice rocker with vigorous stirring for 1 h to prepare the FPD@CD NPs. The NPs were labeled with DiI when PLGA-PEG-PLGA was dissolved in CH_2Cl_2 for confocal laser scanning microscopy (CLSM) and immunofluorescence. We finally prepared various FPD, FPD@C, FPD@CD, FD@CD NPs, and DiI-labeled NPs for different purposes.

2.3. Characterization of the Fe_3O_4-PFH-DiR@CS-DS NPs

The sizes, polydispersity indexes (PDIs), zeta potentials, and encapsulation rates (%) of Fe_3O_4 of the FPD, FPD@C, FPD@CD, and FD@CD NPs were determined. The three-dimensional structure of the FPD@CD NPs was characterized using scanning electron microscopy (SEM, S–3400 N, Hitachi, Ltd., Tokyo, Japan). The dispersion of the DiI-FP@CD NPs was observed using CLSM (A1R, Nikon, Tokyo, Japan). The internal structure of the NPs was observed using a high-resolution transmission electron microscopy (HRTEM, JEM 2100, JEOL Ltd., Tokyo, Japan), FPD or FPD@CD (100 μL, 5 mg mL^{-1}) was diluted in double-distilled water (5 mL), and 1 drop was extracted with a syringe and deposited on a 200-mesh copper grid. Elemental mapping images and energy-dispersive spectroscopy (EDS) line-scan measurements were applied to verify the distribution of iron (Fe), fluorine (F), and sulfur (S) elements in the FPD@CD nanosystem. The mean particle sizes of the FPD@CD NPs dissolved in PBS were measured with prolonged durations (1, 2, 3, 4, 5, 6, and 7 days) using a laser particle size analyzer. The appearance of the FPD@CD NPs solution (5 mg mL^{-1}) was observed with the naked eye. At the same time, we evaluated the *in vitro* US/NIRF/MR imaging capabilities of FPD@CD NPs (Supporting information for detailed methods).

2.4. Cell experiments

2.4.1. Cell culture

RAW 264.7 cells were obtained from the Key Lab of Lipid and Glucose Metabolism of Chongqing Medical University. The cells were cultured with DMEM supplemented with 10% fetal bovine serum and 1% penicillin-streptomycin in a humidified atmosphere containing 5% carbon dioxide (CO_2) at 37 °C. An incubation with lipopolysaccharide (LPS) (100 ng mL^{-1}) for 24 h at 37 °C was performed to activate macrophages and increase their metabolic and phagocytic activity before each cell experiment. All cell culture reagents were provided by Invitrogen (Carlsbad, CA, USA).

2.4.2. In vitro cellular uptake

RAW 264.7 cells were incubated with DiI-FP@CD NPs (1 mg mL^{-1}) for various times (0.5, 2, and 4 h). The cells were washed three times with PBS, fixed with 4% paraformaldehyde for 15 min, and stained with DAPI for another 10 min. Images were collected by CLSM. Fluorescence quantitative maps were calculated using ImageJ software (National Institutes of Health, Bethesda, Maryland, USA). For SEM and transmission electron microscopy (TEM, H-7600, Hitachi, Ltd., Tokyo, Japan), the cells were washed 3 times with PBS and digested with trypsin after incubating with FPD@CD NPs (1 mg mL^{-1}) for 0.5, 2, and 4 h. Cell suspensions were then placed in 1.5-mL pointed Eppendorf (EP) tubes, centrifuged (1000 rpm, 5 min) to produce pellets, fixed with a 2.5% glutaraldehyde fixative solution, dehydrated, and dried with a critical point drier.

2.4.3. In vitro cytotoxicity assay and assessment of the ADV effect

RAW 264.7 cells were seeded in 96-well plates (1×10^4 per well) and incubated with FPD@CD NPs (0, 0.25, 0.5, 1.0, 2.0, 4.0 mg mL^{-1}). After 4, 12, and 24 h of incubation, a standard CCK-8 assay was used to evaluate the viability of the cells.

Then, RAW 264.7 cells were randomly divided into six groups (the control group treated with fresh culture medium, the group subjected to LIFU only, the group treated with FPD@CD NPs only, the group treated with FPD@C NPs combined with LIFU, the group treated with FD@CD NPs combined with LIFU and the group treated with FPD@CD NPs combined with LIFU). The cells in six groups were incubated with the various NPs (1 mg mL^{-1}) for 4 h. Groups combined with LIFU were then

exposed to LIFU irradiation (2.5 W cm^{-2}, 10 min, 1 MHz, 50% duty cycle; The W cm^{-2} represents the spatial average temporal intensity and the peak negative pressure of LIFU used in this study is −0.52 MPa. The ultrasonic probe acts on the bottom of the well plate through the mediation of medical ultrasonic coupling agent. Finally, a CCK-8 assay was implemented to evaluate the viability of the cells. Cells in every group were also harvested for the detection of apoptosis by flow cytometry.

RAW 264.7 cells that had been incubated with FPD@CD NPs (1 mg mL^{-1}) for 4 h were exposed to LIFU at different power intensities (0, 0.5, 2.5, and 4 W cm^{-2} for 10 min, 1 MHz, 50% duty cycle) to further explore the effect of ADV caused by different power intensities of LIFU irradiation. These cells were then incubated with calcein-AM (0.5 mL) diluted in PBS at a ratio of 1:1000 and PI solution (0.5 mL) diluted in PBS at a ratio of 1:500 for 15 min for live-dead cell staining. CLSM was selected to collect images. The cell apoptosis/necrosis ratio (%) was determined using ImageJ software. To observe the morphology, internal microstructure of the cells, and behavior of NPs after irradiation with LIFU at different power intensities by SEM and TEM, scraping the cells gently with a cell scraper, placing the cell suspension in a 1.5-mL pointed EP tube and the sample was centrifuged (1000 rpm, 5 min). The supernatant was aspirated, and 1 mL of a 2.5% glutaraldehyde fixative solution (4 °C) was slowly added. Then, the cells were fixed, dehydrated, and dried with a critical point drier.

2.4.4. In vitro measurement of cytokine levels using ELISAs

The expression and secretion of inflammatory factors (TNF-α, IFN-γ, IL-10, and TGF-β) by macrophages were detected. RAW 264.7 cells were plated in 96-well plates and randomly divided into four groups. Fresh culture medium was added to the control group (100 μL per well). The FPD@C, FD@CD, and FPD@CD NPs (1 mg mL^{-1}, 100 μL per well) were suspended in medium and incubated with cells in the other 3 groups for 4 h. All cells in four groups were then irradiated with LIFU (2.5 W cm^{-2}, 10 min, 1 MHz, 50% duty cycle). The TNF-α, IFN-γ, IL-10, and TGF-β concentrations in the culture medium were measured using ELISAs according to the manufacturer's instructions.

2.5. Animal experiments

2.5.1. Establishment of the optimal animal model of plaques

This study was approved by the Institutional Animal Care and Use Committee at Chongqing Medical University (Chongqing, China), and all experiments were conducted in accordance with the institutional guidelines on the humane care and use of laboratory animals. Normal age-matched wild-type C57BL/6 mice were provided by Chongqing Medical University as the control group and fed a normal diet. Male apoE−/− mice of the C57BL/6J lineage, which were purchased from Beijing Hua Fukang Biotechnology Co., Ltd, were used to establish the model of atherosclerotic plaques.

For the selection of an optimal plaque model, the apoE−/− mice (n = 9) were sacrificed by air embolization after being fed a high-cholesterol diet (D12108C high-fat rodent diet with 1.25% cholesterol, FBSH, Shanghai, China) for 8, 10, or 12 weeks. Digital images of aortic vessels were obtained. The aortas were collected and fixed with 4% paraformaldehyde, and then they were embedded in paraffin and sliced (5 μm). Macrophages in the plaques were detected using immunohistochemical staining with an F4/80 antibody. Images were captured by an optical microscope. The ratio of plaque area to vessel lumen area was quantitatively analyzed using ImageJ software. In subsequent animal experiments, we all selected apoE−/− mice with the optimal plaque model for the experimental group.

2.5.2. Ex vivo plaque binding assay

Normal C57BL/6 mice and apoE−/− model mice were selected to verify the targeting of the FPD@CD NPs to plaques *ex vivo*. After air embolization, the left ventricle of the mouse heart was immediately perfused with normal saline. We dissected the thoracic cavity and peeled off the thoracic aorta (from the root of the aorta to the diaphragm of the descending aorta). The FPD@C and FPD@CD NPs (5 mg mL^{-1}) were incubated with the isolated aorta on a shaker for 4 h at 37 °C. Then, the isolated aortas were washed with PBS three times, further embedded in paraffin and sliced serially (5 μm), stained with a Prussian blue staining solution (20% hydrochloric acid and 10% potassium ferrocyanide solution mixture, 1:1 volume ratio) for 1 h, counterstained with a nuclear fast red solution for 5 min, and washed with distilled water, dehydrated and sealed. Images were acquired with an optical microscope. For immunofluorescence staining, aortas incubated with DiI-FP@CD (5 mg mL^{-1}) on a shaker for 4 h at 37 °C were embedded in optimal cutting temperature compound (OCT) in blocks and placed in a −80 °C freezer. The sections were cut with a cryotome (5 μm) and stained with the F4/80 antibody. Nuclei were counterstained with DAPI. Images were captured with a Nikon Eclipse 80i inverted microscope (Nikon, Tokyo, Japan).

2.5.3. Effect of ADV on plaques ex vivo

The isolated aortas were rinsed with PBS three times after incubating with FPD@CD NPs (5 mg mL^{-1}) on a shaker at 37 °C for 4 h, and then transferred to the agarose mold contained normal saline (37 °C). The samples were irradiated with LIFU at an power intensity of 0.5, 2.5, and 4 W cm^{-2} for 30 min (1 MHz, 50% duty cycle), respectively. All aortas were fixed with 4% paraformaldehyde, embedded in paraffin, and used to generate H&E-stained sections (5 μm). Isolated aortas sections (5 μm) were also obtained for TUNEL assays. Images were captured by an optical microscope and an inverted fluorescence microscope.

2.5.4. In vivo NIRF/MR imaging and plaque binding assay

NIRF and MR imaging were performed on apoE−/− model mice. For NIRF imaging, FPD@CD (targeted group) and FPD@C (non-targeted group) NPs (200 μL, 8 mg mL^{-1}) were administered intravenously via the tail vein (n = 30). Three mice from each group were randomly selected at each time point (0, 0.5, 2, and 4 h, 0 h indicates the time pre-injection), sacrificed by air embolization, and NIRF images of the isolated aortas were acquired. Twenty-four hours after the injection, 3 mice from each group were sacrificed, and fluorescence images of the major organs (heart, liver, spleen, lung, and kidney) were also acquired. The fluorescence intensity was analyzed using Living Image 5.0 software.

For MR imaging, DiI-FP@CD (targeted group) and DiI-FP@C (non-targeted group) NPs (200 μL, 1 mg mL^{-1}) were injected into the model mice (n = 12) and images were captured using a Bruker 7.0-T MRI scanner. The oblique sagittal-sectional T_2*-weighted images of the heart, ascending aorta, and aortic arch region were captured before the injection. The cross-sectional T_2*-weighted images of the ascending aortas were captured at 0, 0.5, 2, and 4 h post-injection. The imaging parameters for the T_2*-weighted gradient-echo were as follows: echo time (TE), 20 ms; repetition time (TR), 400 ms; flip angle (FA), 25°; field of view (FOV), 20 × 20 mm; and slice thickness, 1 mm. Changes in the T_2* signal and the area in which the signal decreased were observed at each time point.

After *in vivo* MRI scans, mice in the two groups were sacrificed by air embolization and the thoracic aortas were removed. Frozen pathological sections (5 μm) were cut for immunofluorescence staining to observe the targeting of the DiI-FP@CD NPs and DiI-FP@C NPs to the macrophages in the plaque. The sections were stained with the F4/80 antibody to detect macrophages, and nuclei were counterstained with DAPI.

2.5.5. Effect of ADV on plaques in vivo

ApoE−/− model mice (n = 30) were housed in a specific pathogen-free room and fed a normal diet throughout the experimental period. The animals were divided into the treatment group and control group. They were treated every 5 days for a total of 4 times. The specific steps are described below. The mice in both groups were anesthetized and fixed to an aseptic operating board in the supine position, and the hair

on the chest and abdomen was removed. FPD@CD NPs (200 μL, 5 mg mL^{-1}) were administered intravenously. At 4 h post-injection, all the mice in the treatment group were irradiated with LIFU (2.5 W cm^{-2}, 30 min, 1 MHz, 50% duty cycle) (probe diameter size 2 cm) above the cardiac region. All the mice in the control group were not subjected to LIFU irradiation.

Before each treatment (0, 5, 10, 15, and 20 d), the procedures described below were performed on the 3 mice randomly selected from all the remaining mice in each group to evaluate the body weight of the mice, the levels of inflammatory factors, and the efficacy of plaque therapy. Blood samples were drawn from the venous plexus using a capillary glass tube with an inner diameter of 1 mm. Then, blood samples were collected into 1.5-mL centrifuge tubes containing EDTA and centrifuged (3000 rpm, 10 min) to separate the red blood cells. The supernatant was extracted to purify the plasma and to determine the concentrations of soluble TNF-α, IFN-γ, IL-10, and TGF-β in the plasma using commercial ELISA kits. The plaque shape, size, and distribution of the entire aorta were observed intuitively through gross pathological specimens. The whole aorta was longitudinally cut and stained with oil red O, and photos of the stained specimens were digitalized for data analysis. The results are presented as the percentage of positive oil red O staining area in the total aorta, which was equivalent to the degree of vascular stenosis.

2.5.6. *In vivo biocompatibility evaluation*

The FPD@CD NPs (200 μL, 10 mg mL^{-1}) were intravenously injected into normal C57BL/6 mice (n = 15). Every three mice were euthanized at different time points (0, 5, 10, 15, and 20 d post-injection), and blood (0.8 mL) was collected for biochemical assays and haematological analysis. Blood biochemical parameters, including the ALT, AST, BUN, CREA, and UA levels, as well as haematological parameters, including the WBC and RBC counts, HGB level, MCV, and PLT counts, were measured. The major organs of the mice (heart, liver, spleen, lung, and kidney) were harvested and fixed with 4% paraformaldehyde for H&E staining.

2.6. *Statistical analysis*

Statistical analyses were conducted using the Statistical Package for the Social Sciences (SPSS; IBM, Armonk, NY, USA). Data were presented as the means ± standard deviations. Student t-tests and one-way ANOVA were used for statistical evaluations. Differences were considered significant at $^{*}P < 0.05$, $^{**}P < 0.01$ and $^{***}P < 0.001$.

3. Results and discussion

3.1. *Characterization of the Fe_3O_4-PFH-DiR@CS-DS NPs*

It has been demonstrated that PEGylation could protect the particles

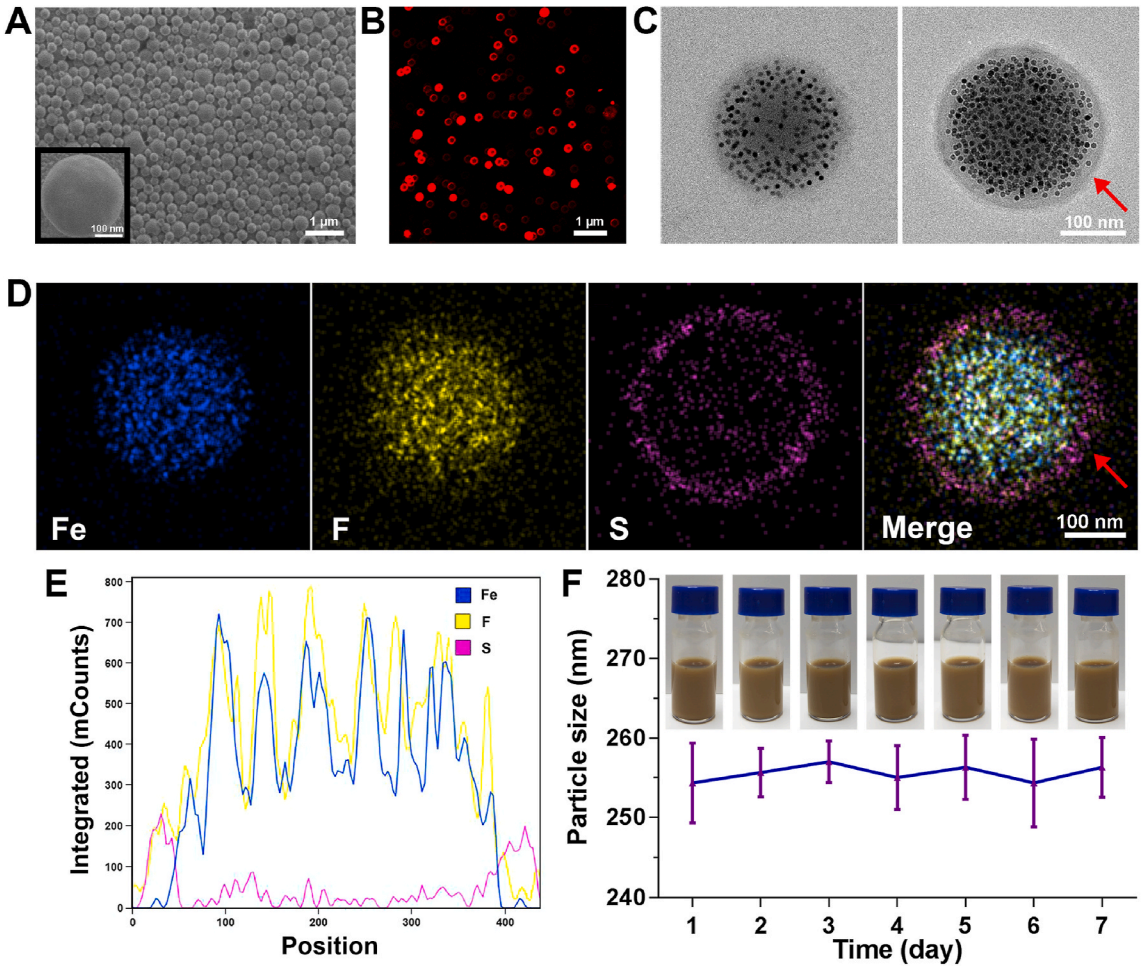

Fig. 1. Characterization of the NPs. SEM and enlarged SEM image (inset) of the FPD@CD NPs (A). CLSM image of DiI-FP@CD NPs (B). HRTEM images of the FPD (left panel) and FPD@CD NPs (right panel); red arrows indicate a distinct ring shape on the surface of the FPD@CD NPs (C). The corresponding elemental mapping of Fe, F, and S and a merged image from HRTEM; red arrows indicate the S element (purple) (D). EDS line-scan mapping of the FPD@CD NPs (E). The size distribution and digital photos of the FPD@CD NPs dispersed in PBS (5 mg mL^{-1}) within 7 days (F).

from rapid phagocytosis by the reticuloendothelial system (RES) *in vivo* and prolong the half-life of particles in plasma [36–38]. The neovascular structure formed in atherosclerotic plaques is incomplete [39,40], and the long-lived circulating NPs of a suitable size are more likely to accumulate in the plaque after transporting through the neovascular structure and penetrating the atherosclerotic plaque. Therefore, PLGA-PEG-PLGA was selected as the carrier material. The sizes, PDIs, zeta potentials, and encapsulation rates of Fe_3O_4 in the FPD, FPD@C, FPD@CD, and FD@CD NPs were listed in Table S1. The FPD@CD NPs displayed a typical spherical shape with a smooth surface and uniform particle size (size of 255.9 ± 2.94 nm and a PDI of 0.097 ± 0.016), as revealed by SEM (Fig. 1A). The DiI-FP@CD NPs exhibited strong red annular fluorescence, homogeneous size, and high dispersion, as detected using CLSM (Fig. 1B). HRTEM images of FPD and FPD@CD NPs (Fig. 1C) showed their individual nanostructures, where oleic acid-modified iron oxide was distributed uniformly inside the whole NPs. A distinct ring shape on the surface of the FPD@CD NPs was observed with the conjugation of CS-DS. The elemental mapping images (Fig. 1D) of Fe (blue) and F (yellow) revealed the co-existence of Fe_3O_4 and PFH. The S element (purple) of dextran sulfate (DS) was annular on the surface of the spherical shell, which was highly consistent with the distribution of DS in the distinct ring shape observed using HRTEM. EDS linear-scanning measurements across the NPs revealed the quantitative relationship of the Fe, F, and S elements in this composite nanosystem (Fig. 1E). The mean particle size of the final NPs showed an ignorable change in PBS, and no aggregation or precipitation phenomenon emerged within 7 days (Fig. 1F), revealing the excellent long-term stability of the obtained NPs.

The phase transition process was observed by US (Fig. S1A) and optical imaging (Fig. S1B). With the extension of the irradiation duration of LIFU, the phase transition became more obvious. The optical images showed the maximum volume of FPD@CD NPs at 10 min, approximately in the range of 2–3 μm. However, part of the NPs ruptured and the concentration of NPs was slightly lower at 20 min, which is consistent with the results of US imaging. In the PFH group (FPD@CD), the acoustic intensity of the B-mode and contrast-enhanced ultrasound (CEUS) images increased gradually, reached a maximum value at 10 min, and decreased at 20 min (Fig. S1C). In contrast, no significant difference in quantitative results was observed for the acoustic intensity of B-mode and CEUS images in the non-PFH group (FD@CD) before and after LIFU irradiation (0, 2, 5, 10, and 20 min) (Fig. S1C). The temperature of NPs was monitored throughout this process (Fig. S1D), which exhibited a slight increase with the extension of time, and the highest temperature as measured was 32 °C in the FPD@CD group, which is lower than the protein denaturation-caused temperature [41]. Thus, thermal damage caused by high temperatures is not a concern in this case. ADV effect is a transient phenomenon when pressure reaches a certain threshold for individual NP [22]. During the cumulative observation time, the countless NPs are constantly undergoing vaporization in which it is a continuous effect. With the prolongation of time, the number of phase-transition NPs increased, so we could observe the change of the US imaging intensity at the macroscopic level. Based on the fact that ultrasonic irradiation could be accompanied by a small amount of heat, the temperature was monitored. Due to the insufficient changes in temperature, the thermal effect is not the main mechanism for vaporization ultimately.

The NIRF images of FPD@CD with different concentrations *in vitro* displayed that the fluorescence intensity increased as the concentration elevated from 0 to 8 mg mL^{-1}. When the concentration was 8 mg mL^{-1}, the fluorescence intensity reached a maximum value of 7.8×10^9 (a.u.). A self-quenching effect and a resulting reduction in the fluorescence intensity were observed accompanying with a further increase in concentration (Fig. S1E). For MR imaging, the T_2* signal intensity decreased gradually with the elevated concentration of FPD@CD NPs (Fig. S1F). In addition, a strong linear correlation was observed between the transverse relaxation rates (R_2*) and concentration. Based on these results, the FPD@CD NPs could serve as the desirable MR contrast agents to effectively reduce the T_2*-weighted signal intensity.

3.2. In vitro results

3.2.1. In vitro cellular uptake

With the prolonging of the incubation time (from 0.5 h to 4 h), more red-stained DiI-FP@CD NPs accumulated around the blue-stained nucleus of RAW 264.7 cells (Fig. 2A). The fluorescence quantitative maps exhibited the strongest red fluorescence intensity around the nucleus at 4 h. SEM images (Fig. 2B) displayed the surface morphology of RAW 264.7 cells. Spherical FPD@CD NPs adhering to the cell membrane surface were observed clearly. At 0.5, 2, and 4 h, the pores in the cell membrane due to endocytosis of NPs were detected. Moreover, TEM images (Fig. 2C) showed that the endocytosed FPD@CD NPs containing dense iron oxide particles were mainly located in the cytoplasmic endocytic vesicles. The number of endocytosed NPs gradually increased and reached a maximum at 4 h, but no DiI-FP@CD NPs were observed in the nucleus, which is consistent with the CLSM results.

3.2.2. In vitro cytotoxicity assay and assessment of the ADV effect

The *in vitro* toxicity of FPD@CD NPs on RAW 264.7 cells and the effect of ADV were explored by a standard CCK-8 assay. The cell viability was still 84% after incubation with 4 mg mL^{-1} FPD@CD NPs for 24 h (Fig. 3A). Different from FPD@C and FD@CD NPs with negligible killing effect, the LIFU-irradiated FPD@CD NPs generated strong cytotoxicity, where the cell viability was only 29% (Fig. 3B). No evident decrease in cell viability was observed in the other groups, which were all higher than 70%. Similar results were obtained by flow cytometry analysis (Fig. 3C). In the FPD@CD combined with LIFU group, the apoptosis rate of the RAW 264.7 cells reached 77.76%, which were all less than 28% in the other groups. When treating RAW 264.7 cells *in vitro* with NPs possessing both targeting and phase transition capabilities, LIFU irradiation must be applied at the same time to exert a significant effect on cell activity. This strategy ensures that the ADV caused by the PFH phase transition specifically occurs in macrophages with NPs. On the contrary, the untargeted areas didn't display a significant decrease in cell activity with LIFU irradiation, ensuring the safety of *in vivo* applications.

At present, the main anti-inflammatory treatment strategies for atherosclerotic plaques focus on blocking monocyte recruitment, increasing macrophage migration, and promoting macrophage apoptosis [42]. A. Bulgarelli et al. [43] confirmed that intravenous injection of methotrexate (MTX) 4 times a week inhibited atherosclerosis in a plaque model of New Zealand rabbits fed a high-fat diet by promoting the migration of macrophages to the intima and apoptosis of macrophages. However, this method by using drugs to induce the apoptosis of macrophages suffers from a slow effect. The systemic treatment with MTX potentially causes adverse effects due to its non-targeted features, such as bone marrow suppression, neutropenia, and infection, which limit its clinical application [44]. Many studies are currently focusing on the specific delivery of drugs in cells to resolve this issue [45,46]. For example, some researchers loaded MTX into a nanosystem formed by lipids and polymer chains. When it was endocytosed by macrophages, it exerted effects inside the macrophages [15]. However, these nanosystems might be trapped in the lysosomes and were unable to be released to exert their functions [47]. Comparatively, the physical effects of ADV adopted in this study were not restricted by endocytotic vesicles or lysosomes. TEM images (Fig. 4A) showed that the FPD@CD NPs in the vesicles of macrophages underwent the liquid-to-gas phase transition and the size increased hundreds of times from the original nanometer level to the micrometer level at 0.5 W cm^{-2} and 2.5 W cm^{-2}. It is noted that the effect of ADV depends on the LIFU intensity. Using live-dead cell staining (Fig. 4B), it can be found that only a small number of macrophages were apoptotic/necrotic (less than 18%) upon exposure to 0.5 W cm^{-2} LIFU irradiation. At 2.5 W cm^{-2}, more macrophages had undergone apoptosis/necrosis (87%). When the

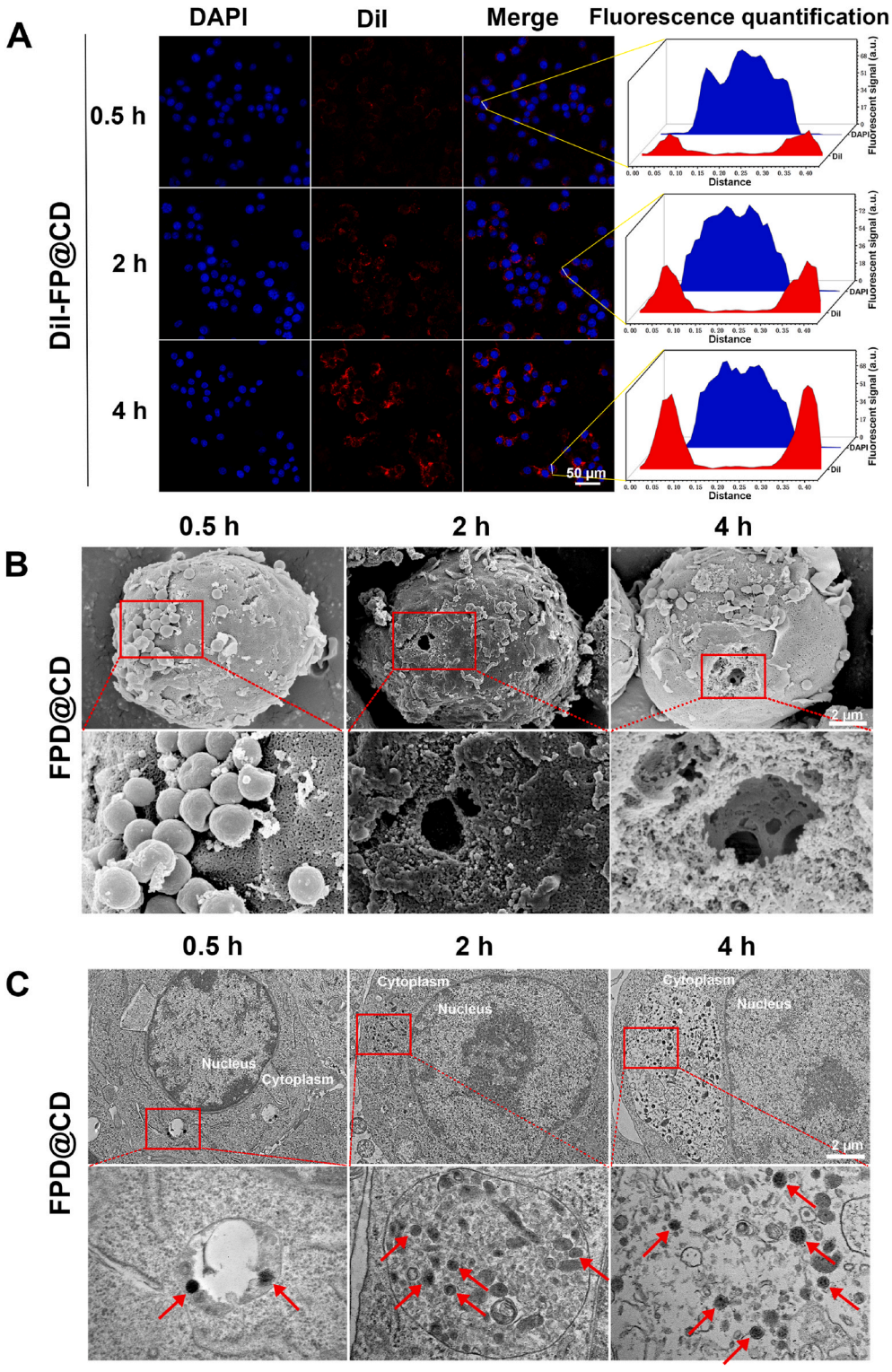

Fig. 2. *In vitro* cellular uptake. CLSM images and the fluorescence quantitative maps of RAW 264.7 cells incubated with the DiI-FP@CD NPs for 0.5, 2, and 4 h (A). SEM images (B) and TEM images (C) of RAW 264.7 cells incubated with the FPD@CD NPs for 0.5, 2, and 4 h. The following line of the image was a higher magnification view of the detailed structures shown in the red box in the above line of the image. The red arrows in the following line of images represented DiI-FP@CD NPs containing dense iron oxide particles.

irradiation power intensity increased to 4 W cm^{-2}, the apoptosis/necrosis rate increased to 100% (Fig. 4A and C).

As shown in TEM images (Fig. 4A), a large number of iron-containing NPs encapsulated by endocytic vesicles without a phase transition were observed in the cell cytoplasm without LIFU irradiation, and the mitochondria were naturally granular or rod-shaped. TEM images of NPs treated with different power densities induced extensive swelling of mitochondria and decreased mitochondria cristae, which was particularly obvious in the 2.5 W cm^{-2} group. The changes in the mitochondrial morphology suggest mitochondrial swelling, which is the most common change of the damaged cells. After exposure to 2.5 W cm^{-2} LIFU irradiation, the apoptotic macrophages with nuclear pyknosis were also observed. However, the collapse of organelle structure, nuclear fragmentation, and the outflow of cell contents were observed after the treatment with 4 W cm^{-2} LIFU. Similar findings were observed by using SEM observation (Fig. 4D), and changes in the degree of cell injury from mild to severe were recorded after exposure to LIFU power intensities of 0, 0.5, 2.5, and 4 W cm^{-2}. The shrunk cell membrane and the altered cell

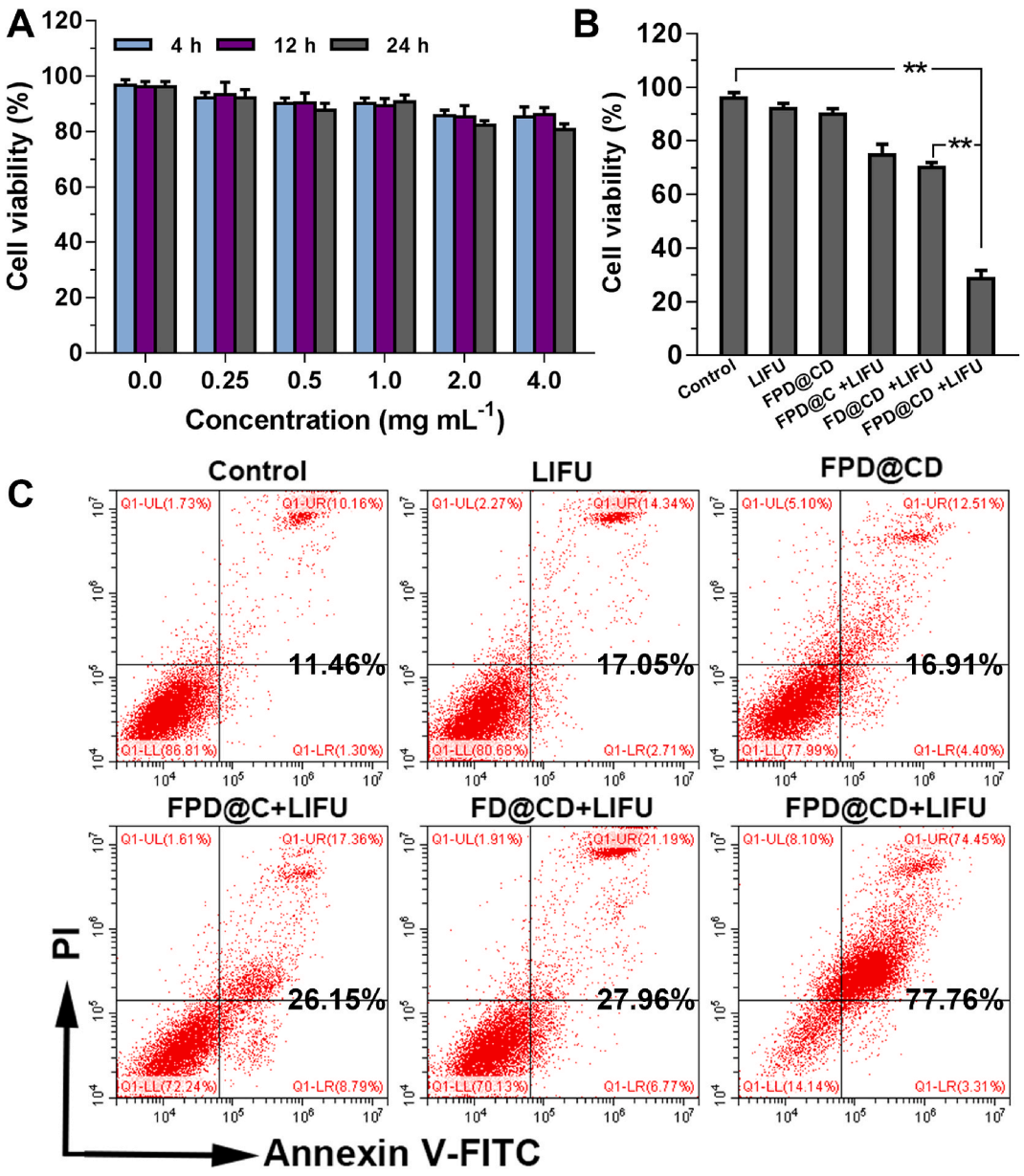

Fig. 3. *In vitro* cytotoxicity assay and assessment of the effect of ADV on RAW 264.7 cells. Relative viability of RAW 264.7 cells after an incubation with various concentrations (0, 0.25, 0.5, 1.0, 2.0 and 4.0 mg mL^{-1}) of the FPD@CD NPs for 4, 12, and 24 h (A). Relative viability of RAW 264.7 cells after different treatments (B). Flow cytometry analysis of cell apoptosis after different treatments (C). (**$P < 0.01$).

morphology were observed after the treatment at 2.5 W cm^{-2} and 4 W cm^{-2}. Comparatively, the fragmentation and decomposition of cells were observed at 4 W cm^{-2} LIFU irradiation. The aforementioned differences in the therapeutic effects could result in the distinct outcomes of vulnerable plaques. Therefore, the most critical factor for the treatment of vulnerable plaques with ADV is the induction of the controllable apoptosis of macrophages. In this work, 2.5 W cm^{-2} was a suitable irradiation power intensity of LIFU at the cellular level.

For clinical purposes, apoptosis is preferable to necrosis because it causes less inflammation, and necrosis often leads to the expansion of the necrotic core and the rupture of the plaque [48]. Phagocytic cells (mainly macrophages) effectively clear apoptotic macrophages, and a reduction in the number of macrophages without the increase of inflammation is an important factor to ensure efficacy. Higher percentages of apoptotic/necrotic macrophages in the plaque could disrupt the phagocytosis and clearance function of the lesion. This may result in the release of a large number of inflammatory substances and promote plaque rupture and severe clinical consequences [49].

3.2.3. *In vitro measurement of cytokine levels using ELISAs*

Monocyte-derived macrophages participate in inflammatory responses by secreting various types of proinflammatory factors, resulting in further inflammatory reactions in atherosclerotic plaques [50]. Thus, macrophages-targeted therapies attenuating the inflammatory response in plaques have been suggested as a possible solution to AS treatment. ELISAs were used to verify the pro/anti-inflammatory effect of FPD@CD NPs. When the cells in four groups were irradiated with LIFU at 2.5 W cm^{-2} for 10 min, significantly lower levels of TNF-α and IFN-γ (pro-inflammatory cytokines) in the FPD@CD group than those in the control, FPD@C and FD@CD groups ($P < 0.05$) were observed (Fig. S2). While the levels of IL-10 and TGF-β (anti-inflammatory cytokines) were 0.091 and 0.094 ng mL^{-1}, respectively, which were significantly higher than the other groups ($P < 0.05$). The induction of macrophage apoptosis could be a stable and effective treatment for vulnerable plaques by

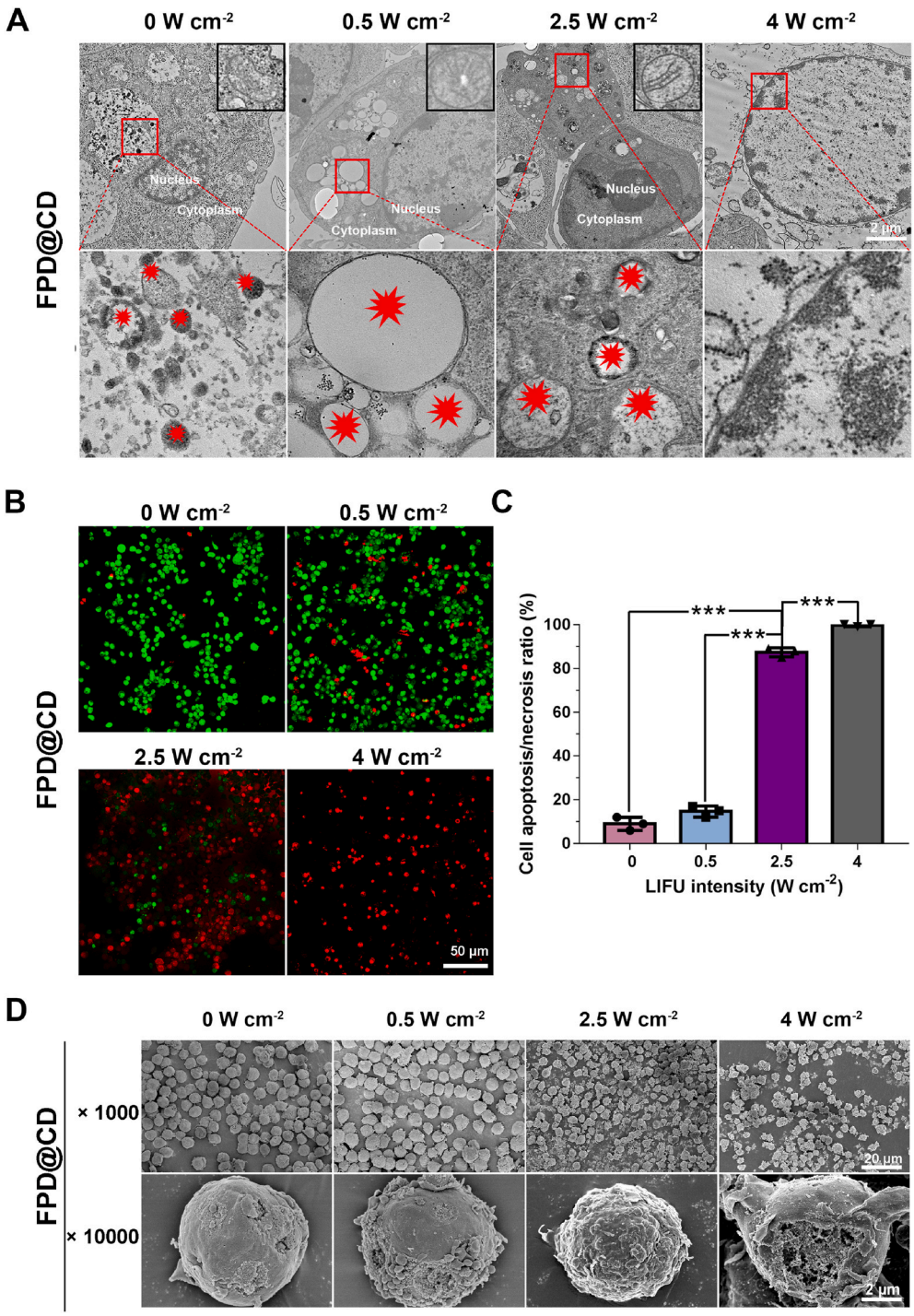

Fig. 4. Effect of ADV on RAW 264.7 cells *in vitro* by LIFU irradiation at different power intensities. TEM images of RAW 264.7 cells treated with the FPD@CD NPs and exposed to LIFU at 0, 0.5, 2.5, and 4 W cm^{-2}. The black box shows a higher magnification image of a representative mitochondrion in the cell. The following line of the TEM image is a higher magnification view of the detailed structures shown in the red box in the above line of image, and red patterns represented FPD@CD NPs that had already or hadn't undergone phase transitions (A). CLSM images of RAW 264.7 cells stained with calcein-AM and PI after treatment with the FPD@CD NPs and exposure to LIFU at 0, 0.5, 2.5, and 4 W cm^{-2} (B). The apoptotic/necrotic ratio (%) of RAW 264.7 cells with different treatments (C). SEM images of RAW 264.7 cells treated with the FPD@CD NPs and exposed to LIFU at 0, 0.5, 2.5, and 4 W cm^{-2} (***$P < 0.001$).

alleviating levels of inflammation.

3.3. Animal experiment results

3.3.1. Establishment of the optimal animal model of plaques

Considering the differences in the composition of early and old plaques, we first verified the morphology and macrophage content of the aortic plaques of the apoE−/− mice fed with a high-cholesterol diet for different durations. Digital images (Fig. S3A) exhibited a difference in the appearance of the aorta after different durations of consumption of a high-cholesterol diet. At the 8th week, the surface of the aorta was smooth and transparently red, and plaques were not observed with the naked eye. At the 10th week, the white plaques were observed from the surface of red blood vessels, and most plaques appeared at the aortic arch and three bifurcations. At the 12th week, many white plaques on the surface of blood vessels were observed with the naked eye, and the walls of the vessels became thicker and uneven. Immunohistochemical staining (Fig. S3B) showed the plaque area at different time points after the initiation of a high-cholesterol diet. In the 400-fold magnified images, the proportion of the plaque area to lumen area at the 10th week was approximately 26%. At the 8th and 12th weeks, the proportions of the plaque area were 7% and 81%, respectively (Fig. S3C). The positive nuclear staining results signified the highest ratio of macrophages on the plaque at 10 weeks, approximately 76.5% (Fig. S3D). The above data

indicate that the mice fed with the high-cholesterol diet for 10 weeks were a suitable animal model for analysis. Therefore, 10 weeks high-cholesterol diet mouse models were chosen in the follow-up *ex vivo* and *in vivo* experiments.

3.3.2. *Ex vivo plaque binding assay*

Prussian blue staining was used to assess the targeting ability of FPD@CD NPs to the plaque by identifying iron co-localization. Considerable Prussian blue deposition was observed in the FPD@CD group of apoE−/− model mice compared with the other groups (Fig. 5A). At the same time, immunofluorescence staining (Fig. 5B) exhibited the presence of plaques, the colocalization of the DiI-FP@CD NPs (red fluorescence) with macrophages (green fluorescence), and the targeted penetration of NPs into the plaque. The colocalization rate quantified by Image J was approximately 86.5%. All results revealed that FPD@CD NPs featured the macrophages-targeted ability and plaque penetration characteristics *ex vivo*.

3.3.3. *Effect of ADV on plaques ex vivo*

H&E and TUNEL staining (Fig. 6A) were further performed to evaluate the therapeutic efficacy of ADV on plaques *ex vivo*. When the LIFU power intensity was set to be 0.5 W cm^{-2}, H&E staining revealed an ignorable change in the plaque morphology, and no apoptotic macrophages emerged in the TUNEL staining. Upon irradiation at 4 W cm^{-2}, H&E images exhibited fissures and holes of various sizes in the plaque area and discontinuity of the fibrous cap, which would inevitably cause plaque rupture and lead to serious clinical outcomes. The TUNEL staining revealed numerous apoptotic cells (green fluorescence). However, when the LIFU power intensity was 2.5 W cm^{-2}, H&E images revealed a negligible change in the morphology and structure of the plaques, and the fibrous caps of plaques remained intact and continuous, but a considerable number of apoptotic cells (green fluorescence) were observed. The TUNEL staining ratios (%) were also quantified (Fig. 6B). The above results demonstrated that different irradiation power intensities induced varied effects on plaques *ex vivo,* among which 2.5 W cm^{-2} was a suitable power intensity.

3.3.4. *In vivo NIRF/MR imaging and plaque binding assay*

The fluorescence intensity at the aortic arch was assessed to validate the active-targeting efficiency *in vivo*. It was subsequently found that this parameter increased in the targeted group (FPD@CD) from 0 to 4 h, and the strongest fluorescence signal of 6.6×10^9 (a.u.) was observed in the aortic arch region at 4 h (Fig. 7A and B). The fluorescence intensity at the aortic arch in the non-targeted group (FPD@C) showed an ignorable change, and only a weak fluorescence signal was observed at 4 h. We harvested the major organs from the two groups at 24 h after the injection. The NPs in both groups mainly accumulated in the liver and spleen (Fig. 7C) due to phagocytosis by the RES and the corresponding fluorescence intensities were quantified (Fig. 7D).

Fig. 7E showed T_2*-weighted MR images of oblique sagittal sections of the heart, ascending aorta, and aortic arch region of the apoE−/− model mice. Cross-sectional T_2*-weighted MR images of the plaque layer of the ascending aortas in the two groups (Fig. 7F) showed a uniform, thin, high-T_2* signal vascular wall and irregular, high-T_2* signal plaques attached to the wall. Over time, a decrease in the T_2* signal was observed of the ascending aortic plaques in the targeted group, indicating that the number of DiI-FP@CD NPs targeted to plaques increased at several time points (0, 0.5, 2, and 4 h). In the non-targeted group, no significant change in the area of high-T_2* signal plaques was observed. The area change rates of high-T2* signal in the plaque area of the two groups from 0 h to 4 h were displayed in Fig. S4. Immunofluorescence staining images (Fig. 7G) in the targeted group displayed the colocalization of the DiI-FP@CD NPs (red fluorescence) with macrophages (green fluorescence). However, few DiI-FP@CD NPs (red fluorescence) were observed in the non-targeted group.

Macrophages are related to the stability of plaques, and plaques with a high macrophage content are often unstable [9,51]. Previous studies [15,52] have demonstrated the passive targeting effects of circulated NPs on plaques because of the low shear stress in the plaque area. In addition, many macrophages are located at the edge of the plaque, particularly vulnerable plaques, which promote the rapid endocytosis of NPs [53]. Based on this passive targeting effect, DS has been introduced to develop the macrophage-specific delivery nanosystem because of its target characteristic. We have observed from *in vitro*, *ex vivo,* and *in vivo* experiments that the NPs were effectively endocytosed by macrophages through this passive and active targeting effect, and their signals were amplified with NIRF and MR for the specific visualization of macrophages and assessment of plaque vulnerability.

3.3.5. *Effect of ADV on plaques in vivo*

According to the results obtained from the cells and *ex vivo* plaque models, LIFU irradiation was acted on the mouse aortic plaque model at the power intensity of 2.5 W cm^{-2}. A schematic is shown in Fig. 8A. Representative images of oil red O staining of gross pathology specimens (Fig. 8B) from the treatment group and control group captured at 0, 5, 10, 15, and 20 days showed that the 20-day LIFU treatment resulted in the desired targeted inhibition of atherosclerotic plaque progression *in vivo*. As shown in Fig. 8C, a 49.4% reduction in the degree of vascular

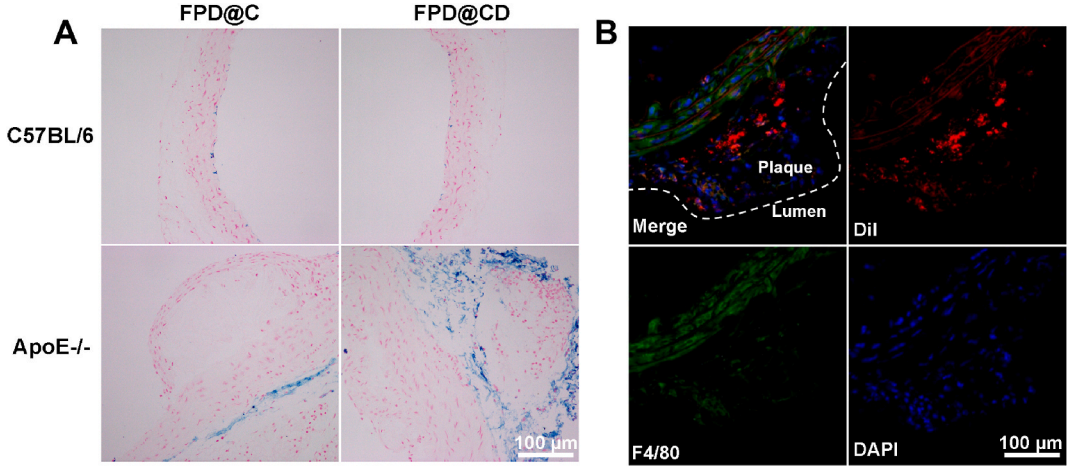

Fig. 5. *Ex vivo* plaque binding assay. Images of Prussian blue-stained sections of isolated aortas (from normal C57BL/6 mice or apoE−/− model mice) incubated with the FPD@C and FPD@CD NPs (5 mg mL^{-1}) for 4 h (A). Images of immunofluorescence staining for the merge signals, DiI-FP@CD NPs (red), F4/80-stained macrophages (green), and DAPI-stained cell nucleus (blue) (B).

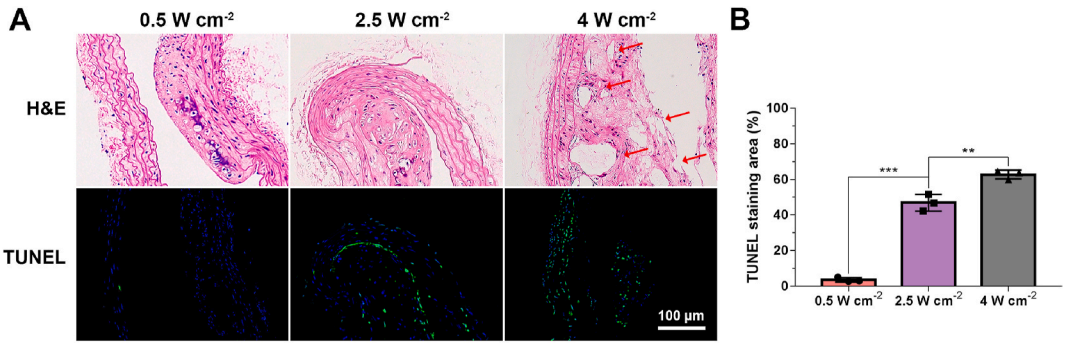

Fig. 6. Effect of ADV on plaques *ex vivo*. H&E staining and TUNEL staining in vulnerable plaques subjected to LIFU irradiation at different power intensities (0.5, 2.5, and 4 W cm^{-2}) for 30 min. Red arrows show pores of various sizes in the plaque area and the discontinuity of the fiber cap (A). TUNEL staining area (%) in different groups (B). (**$P < 0.01$, ***$P < 0.001$).

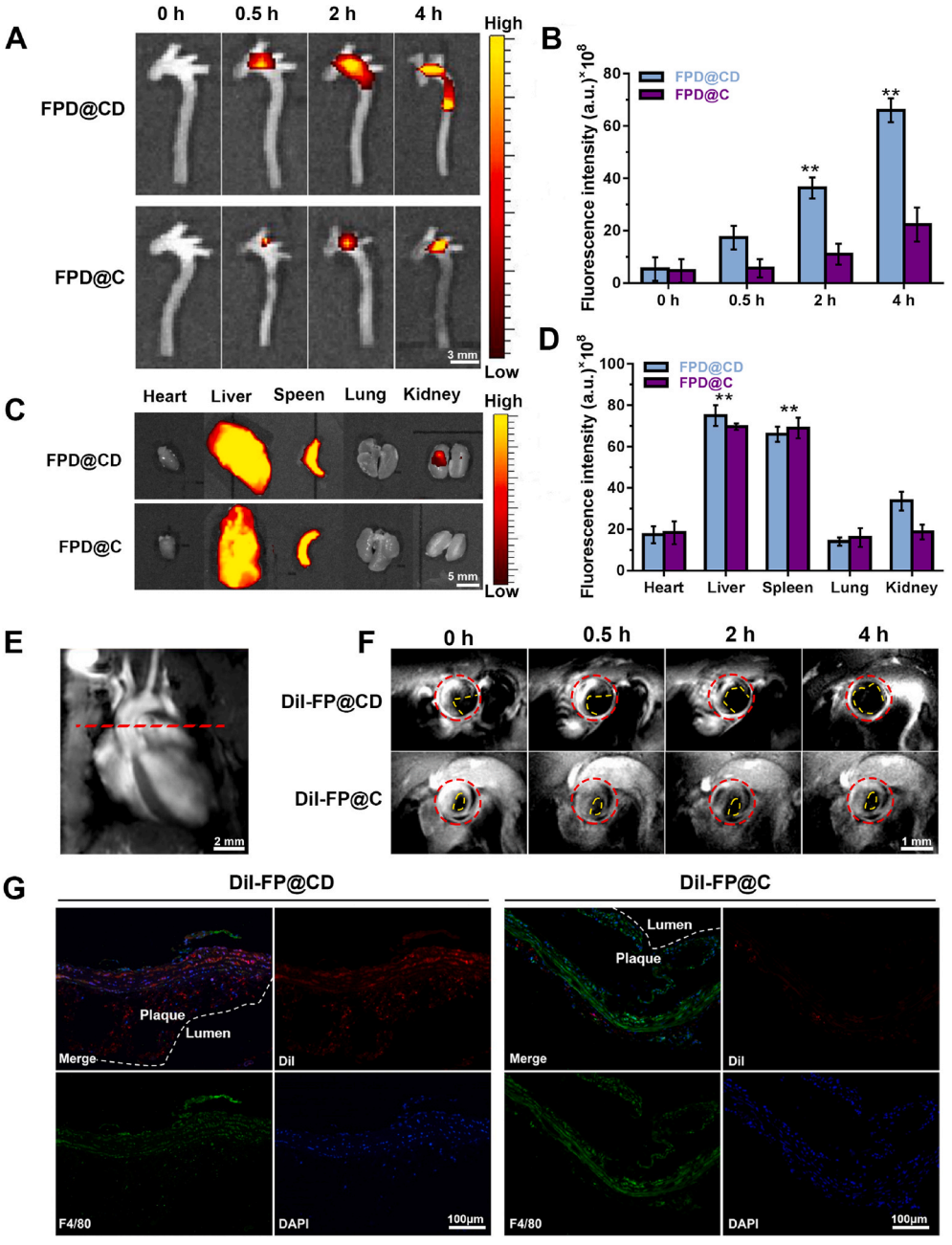

Fig. 7. *In vivo* NIRF/MR imaging and plaque binding assay. NIRF images (A) and fluorescence intensity (B) of the aortic arch from apoE−/− mice at 0, 0.5, 2, and 4 h post-injection in the targeted group and non-targeted group. NIRF images (C) and fluorescence intensity (D) of the major organs from the two groups at 24 h post-injection. Oblique sagittal-sectional T_2*-weighted images of the heart, ascending aorta, and aortic arch region of the apoE−/− model mice. The red dotted line is the scanning location line (E). Cross-sectional T_2*-weighted images of the plaque layer of the ascending aortas of the apoE−/− mice in the targeted and non-targeted group at 0, 0.5, 2, and 4 h. The red dotted line represents the high-T_2* signal vascular wall, and the yellow dotted area represents the irregular and low-T_2* signal area in the vascular lumen (F). Images of immunofluorescence staining in the two groups were obtained after MR imaging *in vivo* (G). (**$P < 0.01$).

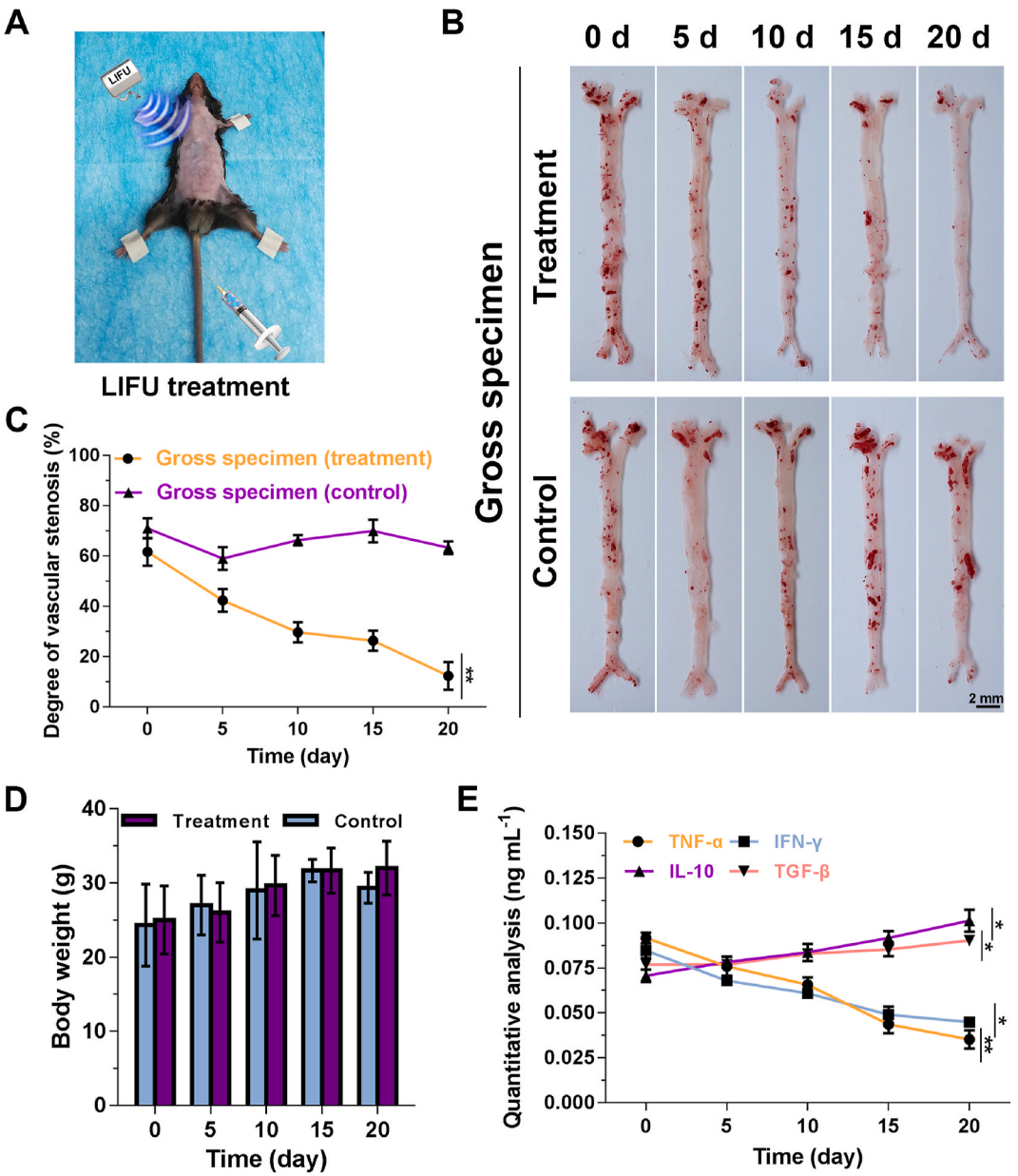

Fig. 8. Effect of ADV on plaques *in vivo*. A schematic of the LIFU treatment (A). Representative images (0, 5, 10, 15, and 20 d) of oil red O staining in gross specimens of the treatment group (FPD@CD NPs with LIFU irradiation) and control group (FPD@CD NPs without LIFU irradiation) (B). The degree of vascular stenosis in gross specimens from the two groups (C). Body weight of the apoE−/− mice in two groups (D). The levels of pro-inflammatory factors (TNF-α and IFN-γ) and anti-inflammatory factors (IL-10 and TGF-β) in the treatment group were measured at different time points using ELISAs (E). (*$P < 0.05$ and **$P < 0.01$).

stenosis (61.7% at day 0 *vs*.12.3% at day 20) in gross pathology specimens was observed throughout the treatment period. In the control group, no trend of a reduction in the degree of vascular stenosis was observed within 20 days. The body weight of the mice was also recorded, and no abnormalities were observed during the 20 days in both groups (Fig. 8D). In addition, the levels of TNF-α and IFN-γ in the plasma decreased, while the levels of IL-10 and TGF-β increased over time in the treatment group throughout the course of treatment (Fig. 8E). The use of ADV to induce macrophage apoptosis as a treatment for vulnerable plaques features some advantages compared with conventional clinical treatment methods. Drugs must be taken for a long time, and their effects on plaques are not clear, thus, their ability to reduce and reverse plaques is difficult. Compared with the interventional and surgical treatment, the developed strategy in this work is less invasive, even for the plaques located in the small blood vessels, which is still effective.

3.3.6. *In vivo biocompatibility evaluation*

The toxicity of FPD@CD NPs *in vivo* was also investigated systematically. No deaths were observed over 20 days. When comparing the biochemical analyses and hematological parameters (0, 5, 10, 15, and 20 d post-injection), all indicator values were within the normal range (Figs. S5A and S5B). The histological results of the major organs, including the heart, liver, spleen, lung, and kidney, exhibited no adverse effects (Fig. S5C). Based on these biosafety evaluation results, it can be demonstrated that the prepared NPs were safe at the tested dose (10 mg mL^{-1}) in mice, and no cases of infection, inflammation, or liver or kidney dysfunction were observed.

4. Conclusions

In summary, LIFU-responsive nanomedicine for stabilizing vulnerable atherosclerotic plaques was rationally designed and successfully

constructed in this work. PFH, Fe_3O_4, and DiR were co-loaded into the hollow PLGA-PEG-PLGA NPs, and the targeting agent DS was attached to the surface of the NPs. The final FPD@CD NPs exhibited superior targeting performance to vulnerable plaques through passive and active effects. Controlled apoptosis rather than necrosis of macrophages was induced through the regulation of LIFU intensity, which might be attributed to mitochondrial damage. In the treatment of vulnerable plaques *in vivo*, the introduced ADV effect could stabilize and reduce the plaque, which could be visualized and evaluated with NIRF and MR imaging. Therefore, the ADV effect caused by LIFU irradiation performed conveniently and generated little trauma. This treatment not only reduced the risk of plaque rupture but also decreased the stenosis of blood vessels and restored hemodynamics to a certain extent, avoiding acute cardiovascular and cerebrovascular events, which represents major benefits for patients with cardiovascular and cerebrovascular diseases.

Declaration of competing interest

The authors declare no competing financial interest.

CRediT authorship contribution statement

Jingxin Hou: Conceptualization, Methodology, Investigation, Writing – original draft. **Jun Zhou:** Conceptualization, Methodology, Investigation, Writing – original draft. **Meiqi Chang:** Investigation, Writing – review & editing. **Guangcheng Bao:** Investigation, Visualization. **Jie Xu:** Investigation, Visualization. **Man Ye:** Visualization. **Yixin Zhong:** Visualization. **Shuling Liu:** Visualization. **Junrui Wang:** Investigation. **Wei Zhang:** Supervision. **Haitao Ran:** Supervision. **Zhigang Wang:** Supervision, Writing – review & editing, Funding acquisition. **Yu Chen:** Conceptualization, Supervision, Writing – review & editing, Funding acquisition. **Dajing Guo:** Supervision, Writing – review & editing, Funding acquisition.

Acknowledgements

The authors gratefully acknowledge financial support from the National Natural Science Foundation of China (Grant Nos. 81701650, 81971608, and 82172092), the Kuanren Talents Program of the Second Affiliated Hospital of Chongqing Medical University (Grant No. 2020-7) and the Science & Technology Commission Foundation of Chongqing (Grant No. cstc2017jcyjAX0444).

Appendix A. Supplementary data

Supplementary data to this article can be found online at https://doi.org/10.1016/j.bioactmat.2022.02.022.

References

[1] C. Woolston, How RNA therapies could be used to tackle the world's biggest killer, Nature 574 (7778) (2019) 13–14.
[2] B. Cannon, Cardiovascular disease: biochemistry to behaviour, Nature 493 (7434) (2013) 2–3.
[3] A.R. Tall, R.L. Levine, Cardiovascular disease: commonality with cancer, Nature 543 (7643) (2017) 45–47.
[4] Y. Shi, Y. Gao, X. Zou, L. Chen, Y. Li, Imaging of carotid artery inflammatory plaques with superparamagnetic nanoparticles and an external magnet collar, J. Mater. Chem. B 5 (4) (2017) 797–806.
[5] A.M. Noyes, P.D. Thompson, A systematic review of the time course of atherosclerotic plaque regression, Atherosclerosis 234 (1) (2014) 75–84.
[6] F. Mach, C. Baigent, A.L. Catapano, K.C. Koskinas, M. Casula, L. Badimon, M. J. Chapman, G.G. De Backer, V. Delgado, B.A. Ference, I.M. Graham, A. Halliday, U. Landmesser, B. Mihaylova, T.R. Pedersen, G. Riccardi, D.J. Richter, M. S. Sabatine, M.R. Taskinen, L. Tokgozoglu, O. Wiklund, 2019 ESC/EAS guidelines for the management of dyslipidaemias: lipid modification to reduce cardiovascular risk, Eur. Heart J. 41 (1) (2020) 111–188.
[7] B. Banik, B. Surnar, B.W. Askins, M. Banerjee, S. Dhar, Dual-targeted synthetic nanoparticles for cardiovascular diseases, ACS Appl. Mater. Interfaces 12 (6) (2020) 6852–6862.
[8] Y.J. Zhang, D.N. Bai, J.X. Du, L. Jin, J. Ma, J.L. Yang, W.B. Cai, Y. Feng, C.Y. Xing, L.J. Yuan, Y.Y. Duan, Ultrasound-guided imaging of junctional adhesion molecule-A-targeted microbubbles identifies vulnerable plaque in rabbits, Biomaterials 94 (2016) 20–30.
[9] H. Qiao, Y. Wang, R. Zhang, Q. Gao, X. Liang, L. Gao, Z. Jiang, R. Qiao, D. Han, Y. Zhang, Y. Qiu, J. Tian, M. Gao, F. Cao, MRI/optical dual-modality imaging of vulnerable atherosclerotic plaque with an osteopontin-targeted probe based on Fe (3)O(4) nanoparticles, Biomaterials 112 (2017) 336–345.
[10] Q. Wei, J. Wang, W. Shi, B. Zhang, H. Jiang, M. Du, H. Mei, Y. Hu, Improved *in vivo* detection of atherosclerotic plaques with a tissue factor-targeting magnetic nanoprobe, Acta Biomater. 90 (2019) 324–336.
[11] R.A. Chmielowski, D.S. Abdelhamid, J.J. Faig, L.K. Petersen, C.R. Gardner, K. E. Uhrich, L.B. Joseph, P.V. Moghe, Athero-inflammatory nanotherapeutics: Ferulic acid-based poly(anhydride-ester) nanoparticles attenuate foam cell formation by regulating macrophage lipogenesis and reactive oxygen species generation, Acta Biomater. 57 (2017) 85–94.
[12] J. Tang, M.E. Lobatto, L. Hassing, S. van der Staay, S.M. van Rijs, C. Calcagno, M. S. Braza, S. Baxter, F. Fay, B.L. Sanchez-Gaytan, R. Duivenvoorden, H. Sager, Y. M. Astudillo, W. Leong, S. Ramachandran, G. Storm, C. Pérez-Medina, T. Reiner, D. P. Cormode, G.J. Strijkers, E.S. Stroes, F.K. Swirski, M. Nahrendorf, E.A. Fisher, Z. A. Fayad, W.J. Mulder, Inhibiting macrophage proliferation suppresses atherosclerotic plaque inflammation, Sci. Adv. 1 (3) (2015).
[13] Y. Ma, Y. Ma, M. Gao, Z. Han, W. Jiang, Y. Gu, Y. Liu, Platelet-mimicking therapeutic system for noninvasive mitigation of the progression of atherosclerotic plaques, Adv. Sci. 8 (8) (2021) 2004128.
[14] R. Duivenvoorden, J. Tang, D.P. Cormode, A.J. Mieszawska, D. Izquierdo-Garcia, C. Ozcan, M.J. Otten, N. Zaidi, M.E. Lobatto, S.M. van Rijs, B. Priem, E.L. Kuan, C. Martel, B. Hewing, H. Sager, M. Nahrendorf, G.J. Randolph, E.S. Stroes, V. Fuster, E.A. Fisher, Z.A. Fayad, W.J. Mulder, A statin-loaded reconstituted high-density lipoprotein nanoparticle inhibits atherosclerotic plaque inflammation, Nat. Commun. 5 (2014) 3065.
[15] C. Stigliano, M.R. Ramirez, J.V. Singh, S. Aryal, J. Key, E. Blanco, P. Decuzzi, Methotraxate-loaded hybrid nanoconstructs target vascular lesions and inhibit atherosclerosis progression in ApoE(-/-) mice, Adv. Healthcare Mater. 6 (13) (2017).
[16] W. Kałas, E. Wysokińska, M. Przybyło, M. Langner, A. Ulatowska-Jarża, D. Biały, M. Wawrzyńska, E. Zioło, W. Gil, A.M. Trzeciak, H. Podbielska, M. Kopaczyńska, Photoactive liposomal formulation of PVP-conjugated chlorin e6 for photodynamic reduction of atherosclerotic plaque, Int. J. Mol. Sci. 20 (16) (2019).
[17] V.N. Nguyen, Y. Yan, J. Zhao, J. Yoon, Heavy-atom-free photosensitizers: from molecular design to applications in the photodynamic therapy of cancer, Accounts Chem. Res. 54 (1) (2021) 207–220.
[18] Z. Li, Y. Liu, L. Chen, X. Hu, Z. Xie, A glutathione-activatable photodynamic and fluorescent imaging monochromatic photosensitizer, J. Mater. Chem. B 5 (22) (2017) 4239–4245.
[19] L. Zhang, H. Yi, J. Song, J. Huang, K. Yang, B. Tan, D. Wang, N. Yang, Z. Wang, X. Li, Mitochondria-targeted and ultrasound-activated nanodroplets for enhanced deep-penetration sonodynamic cancer therapy, ACS Appl. Mater. Interfaces 11 (9) (2019) 9355–9366.
[20] Z. Teng, R. Wang, Y. Zhou, M. Kolios, Y. Wang, N. Zhang, Z. Wang, Y. Zheng, G. Lu, A magnetic droplet vaporization approach using perfluorohexane-encapsulated magnetic mesoporous particles for ultrasound imaging and tumor ablation, Biomaterials 134 (2017) 43–50.
[21] M. Ye, J. Zhou, Y. Zhong, J. Xu, J. Hou, X. Wang, Z. Wang, D. Guo, SR-A-targeted phase-transition nanoparticles for the detection and treatment of atherosclerotic vulnerable plaques, ACS Appl. Mater. Interfaces 11 (10) (2019) 9702–9715.
[22] O.D. Kripfgans, J.B. Fowlkes, D.L. Miller, O.P. Eldevik, P.L. Carson, Acoustic droplet vaporization for therapeutic and diagnostic applications, Ultrasound Med. Biol. 26 (7) (2000) 1177–1189.
[23] L. Zhu, H. Zhao, Z. Zhou, Y. Xia, Z. Wang, H. Ran, P. Li, J. Ren, Peptide-functionalized phase-transformation nanoparticles for low intensity focused ultrasound-assisted tumor imaging and therapy, Nano Lett. 18 (3) (2018) 1831–1841.
[24] Y. Zhong, Y. Zhang, J. Xu, J. Zhou, J. Liu, M. Ye, L. Zhang, B. Qiao, Z.G. Wang, H. T. Ran, D. Guo, Low-intensity focused ultrasound-responsive phase-transitional nanoparticles for thrombolysis without vascular damage: a synergistic nonpharmaceutical strategy, ACS Nano 13 (3) (2019) 3387–3403.
[25] J. Xu, J. Zhou, Y. Zhong, Y. Zhang, J. Liu, Y. Chen, L. Deng, D. Sheng, Z. Wang, H. Ran, D. Guo, Phase transition nanoparticles as multimodality contrast agents for the detection of thrombi and for targeting thrombolysis: *in vitro* and *in vivo* experiments, ACS Appl. Mater. Interfaces 9 (49) (2017) 42525–42535.
[26] Y. Zhou, Z. Wang, Y. Chen, H. Shen, Z. Luo, A. Li, Q. Wang, H. Ran, P. Li, W. Song, Z. Yang, H. Chen, Z. Wang, G. Lu, Y. Zheng, Microbubbles from gas-generating perfluorohexane nanoemulsions for targeted temperature-sensitive ultrasonography and synergistic HIFU ablation of tumors, Adv. Mater. 25 (30) (2013) 4123–4130.
[27] C.H. Fan, Y.T. Lin, Y.J. Ho, C.K. Yeh, Spatial-temporal cellular bioeffects from acoustic droplet vaporization, Theranostics 8 (20) (2018) 5731–5743.
[28] L.A. Davis, S.E. Stewart, C.G. Carsten 3rd, B.A. Snyder, M.A. Sutton, S.M. Lessner, Characterization of fracture behavior of human atherosclerotic fibrous caps using a miniature single edge notched tensile test, Acta Biomater. 43 (2016) 101–111.

[29] S. Srettabunjong, Ascending aortic rupture through a penetrating atherosclerotic ulcer: a rare cause of sudden unexpected death, J. Forensic Sci. 63 (2) (2018) 608–610.
[30] L. Zhang, H. Yi, J. Song, J. Huang, K. Yang, B. Tan, D. Wang, N. Yang, Z. Wang, X. Li, Mitochondria-targeted and ultrasound-activated nanodroplets for enhanced deep-penetration sonodynamic cancer therapy, ACS Appl. Mater. Interfaces 11 (9) (2019) 9355–9366.
[31] Y. Zhou, R. Wang, Z. Teng, Z. Wang, B. Hu, M. Kolios, H. Chen, N. Zhang, Y. Wang, P. Li, X. Wu, G. Lu, Y. Chen, Y. Zheng, Magnetic nanoparticle-promoted droplet vaporization for *in vivo* stimuli-responsive cancer theranostics, NPG Asia Mater. 8 (2016).
[32] C.S. Kwok, W. Hulme, I. Olier, E. Holroyd, M.A. Mamas, Review of early hospitalisation after percutaneous coronary intervention, Int. J. Cardiol. 227 (2017) 370–377.
[33] X. Wei, M. Ying, D. Dehaini, Y. Su, A.V. Kroll, J. Zhou, W. Gao, R.H. Fang, S. Chien, L. Zhang, Nanoparticle functionalization with platelet membrane enables multifactored biological targeting and detection of atherosclerosis, ACS Nano 12 (1) (2018) 109–116.
[34] X. Chen, Y. Zhang, H. Zhang, L. Zhang, L. Liu, Y. Cao, H. Ran, J. Tian, A non-invasive nanoparticles for multimodal imaging of ischemic myocardium in rats, J. Nanobiotechnol. 19 (1) (2021) 82.
[35] J. Liu, B. Zhou, Y. Guo, A. Zhang, K. Yang, Y. He, J. Wang, Y. Cheng, D. Cui, SR-A-targeted Nanoplatform for Sequential Photothermal/photodynamic Ablation of Activated Macrophages to Alleviate Atherosclerosis, ACS applied materials & interfaces, 2021.
[36] X. Song, H. Gong, T. Liu, L. Cheng, C. Wang, X. Sun, C. Liang, Z. Liu, J-aggregates of organic dye molecules complexed with iron oxide nanoparticles for imaging-guided photothermal therapy under 915-nm light, Small 17 (2) (2021), e2007013.
[37] D. Selli, M. Tawfilas, M. Mauri, R. Simonutti, C. Di Valentin, Optimizing PEGylation of TiO(2) nanocrystals through a combined experimental and computational study, Chem. Mater. 31 (18) (2019) 7531–7546.
[38] Y. Zhu, C. Chen, Z. Cao, S. Shen, L. Li, D. Li, J. Wang, X. Yang, On-demand PEGylation and dePEGylation of PLA-based nanocarriers via amphiphilic mPEG-TK-Ce6 for nanoenabled cancer chemotherapy, Theranostics 9 (26) (2019) 8312–8320.
[39] P.R. Moreno, K.R. Purushothaman, E. Zias, J. Sanz, V. Fuster, Neovascularization in human atherosclerosis, Curr. Mol. Med. 6 (5) (2006) 457–477.
[40] K.S. Moulton, K. Vakili, D. Zurakowski, M. Soliman, C. Butterfield, E. Sylvin, K. M. Lo, S. Gillies, K. Javaherian, J. Folkman, Inhibition of plaque neovascularization reduces macrophage accumulation and progression of advanced atherosclerosis, Proc. Natl. Acad. Sci. U.S.A. 100 (8) (2003) 4736–4741.
[41] M.P. Calatayud, E. Soler, T.E. Torres, E. Campos-Gonzalez, C. Junquera, M. R. Ibarra, G.F. Goya, Cell damage produced by magnetic fluid hyperthermia on microglial BV2 cells, Sci. Rep. 7 (1) (2017) 8627.
[42] X. Zang, M. Cheng, X. Zhang, X. Chen, Targeting macrophages using nanoparticles: a potential therapeutic strategy for atherosclerosis, J. Mater. Chem. B 9 (15) (2021) 3284–3294.
[43] A. Bulgarelli, A.A. Martins Dias, B. Caramelli, R.C. Maranhão, Treatment with methotrexate inhibits atherogenesis in cholesterol-fed rabbits, J. Cardiovasc. Pharmacol. 59 (4) (2012) 308–314.
[44] K. Schmiegelow, Advances in individual prediction of methotrexate toxicity: a review, Br. J. Haematol. 146 (5) (2009) 489–503.
[45] A.N. Ramya, M.M. Joseph, S. Maniganda, V. Karunakaran, T.T. Sreelekha, K. K. Maiti, Emergence of gold-mesoporous silica hybrid nanotheranostics: Dox-encoded, folate targeted chemotherapy with modulation of SERS fingerprinting for apoptosis toward tumor eradication, Small 17 (2) (2021), e2007852.
[46] F.L.T. Gomes, R.C. Maranhão, E.R. Tavares, P.O. Carvalho, M.L. Higuchi, F. R. Mattos, F.G. Pitta, S.A. Hatab, R. Kalil-Filho, C.V. Serrano Jr., Regression of atherosclerotic plaques of cholesterol-fed rabbits by combined chemotherapy with paclitaxel and methotrexate carried in lipid core nanoparticles, J. Cardiovasc. Pharmacol. Therapeut. 23 (6) (2018) 561–569.
[47] M. Tan, W. Liu, F. Liu, W. Zhang, H. Gao, J. Cheng, Y. Chen, Z. Wang, Y. Cao, H. Ran, Silk fibroin-coated nanoagents for acidic lysosome targeting by a functional preservation strategy in cancer chemotherapy, Theranostics 9 (4) (2019) 961–973.
[48] C. Geng, Y. Zhang, T.H. Hidru, L. Zhi, M. Tao, L. Zou, C. Chen, H. Li, Y. Liu, Sonodynamic therapy: a potential treatment for atherosclerosis, Life Sci. 207 (2018) 304–313.
[49] I. Tabas, Consequences and therapeutic implications of macrophage apoptosis in atherosclerosis: the importance of lesion stage and phagocytic efficiency, Arterioscler. Thromb. Vasc. Biol. 25 (11) (2005) 2255–2264.
[50] Y. Jiang, J. Kou, X. Han, X. Li, Z. Zhong, Z. Liu, Y. Zheng, Y. Tian, L. Yang, ROS-dependent Activation of Autophagy through the PI3K/Akt/mTOR Pathway Is Induced by Hydroxysafflor Yellow A-Sonodynamic Therapy in THP-1 Macrophages, Oxidative Medicine and Cellular Longevity, 2017, 2017, p. 8519169.
[51] Y. Narita, K. Shimizu, K. Ikemoto, R. Uchino, M. Kosugi, M.B. Maess, Y. Magata, N. Oku, M. Ogawa, Macrophage-targeted, enzyme-triggered fluorescence switch-on system for detection of embolism-vulnerable atherosclerotic plaques, J. Contr. Release 302 (2019) 105–115.
[52] S.S. Hossain, Y. Zhang, X. Fu, G. Brunner, J. Singh, T.J. Hughes, D. Shah, P. Decuzzi, Magnetic resonance imaging-based computational modelling of blood flow and nanomedicine deposition in patients with peripheral arterial disease, J. R. Soc. Interface 12 (106) (2015).
[53] V. Bagalkot, M.A. Badgeley, T. Kampfrath, J.A. Deiuliis, S. Rajagopalan, A. Maiseyeu, Hybrid nanoparticles improve targeting to inflammatory macrophages through phagocytic signals, J. Contr. Release 217 (2015) 243–255.